

Large-eddy simulation of vortex streets and pollutant dispersion behind high-rise buildings

Beom-Soon Han,^a Seung-Bu Park,^{a,b} Jong-Jin Baik,^{a*} Junho Park^a and Kyung-Hwan Kwak^c

^a*School of Earth and Environmental Sciences, Seoul National University, Seoul, South Korea*

^b*Department of Earth and Environmental Engineering, Columbia University, New York, NY, USA*

^c*School of Natural Resources and Environmental Science, Kangwon National University, Chuncheon, South Korea*

*Correspondence to: J.-J. Baik, School of Earth and Environmental Sciences, Seoul National University, 1 Gwanak-ro, Gwanak-gu, Seoul 08826, South Korea. E-mail: jjbaik@snu.ac.kr

Understanding turbulent flow and pollutant dispersion in urban areas is one of the important problems in urban meteorology and environmental fluid mechanics. In this study, we examine turbulent flow and pollutant dispersion in a densely built-up area in Seoul, South Korea, using the parallelized large-eddy simulation model (PALM). In particular, we focus on vortex streets and associated pollutant dispersion behind high-rise buildings. The turbulence recycling method is used to produce inflow profiles. Vortices are generated near the high-rise buildings and propagate downstream forming vortex streets behind the high-rise buildings. To investigate characteristics of the vortex streets, spectral and correlation analyses are performed. The spectral analysis reveals that vortices have a non-dimensional vortex shedding frequency of 0.1–0.2, and this periodicity is weakened due to the influence of other buildings. The correlation analysis shows that vortices appear frequently in regions of negative pressure perturbation. The vertical turbulent momentum fluxes induced by ejections and sweeps largely contribute to the total vertical turbulent momentum flux downstream of the high-rise buildings. Especially, ejections in the wake region are stronger compared to other regions because ejections are induced by vortices near the top of the high-rise buildings. It is found that pollutant dispersion is interrupted by both low-rise and high-rise buildings. Strong updraughts behind the high-rise buildings transport pollutant upward and increase the mean pollutant concentration at upper levels. Vortices forming the vortex streets play a role in pollutant mixing in such a way that the vortices eject air of high pollutant concentration from the wake region behind the high-rise buildings and entrain air of low pollutant concentration into the wake region. The mixing by vortices is verified by the correlation between vorticity and pollutant concentration.

Key Words: vortex streets; pollutant dispersion; wake; ejection; sweep; high-rise buildings; large-eddy simulation

Received 17 May 2016; Revised 22 June 2017; Accepted 7 July 2017; Published online in Wiley Online Library 30 August 2017

1. Introduction

Many investigations have been devoted to better understanding of flow and pollutant dispersion in urban areas (e.g. Britter and Hanna, 2003; Rotach *et al.*, 2004; Edussuriya *et al.*, 2011; Nakayama *et al.*, 2013; Panagiotou *et al.*, 2013). One of the crucial factors that affect flow and pollutant dispersion in urban areas is buildings. In particular, high-rise buildings modify flow and pollutant dispersion significantly. Wind-tunnel experiments (Heist *et al.*, 2004, 2009) and observation studies in real urban areas (Gowardhan *et al.*, 2007; Nelson *et al.*, 2007; Hanna and Chang, 2015) revealed that updraughts occurring behind high-rise buildings transport pollutants upward. Moreover, vortices generated continuously on both sides of high-rise buildings, a phenomenon known as vortex shedding, propagate downstream of the high-rise buildings and affect flow and pollutant dispersion.

A high-rise building can be simplified as a column of a tall height mounted on a flat surface, and there have been many studies on flow structures behind the column (e.g. Fröhlich and Rodi, 2004; Palau-Salvador *et al.*, 2010; Sattari *et al.*, 2012; Sumner, 2013). Kawamura *et al.* (1984) experimentally studied flow around a finite-height circular column and observed that a pair of trailing vortices are shed at the top of the column and interact with the downwash flow behind the column. They pointed out that no periodic vortex shedding occurs if the ratio H/d is smaller than a critical value where H and d are the column height and width, respectively (see also Sumner *et al.* (2004)). More detailed results were presented for a finite-height square column by Wang and his co-workers who performed experiments on flow structures around the square column for different H/d (Wang *et al.*, 2004, 2006; Wang and Zhou, 2009). Wang *et al.* (2004) found that for small H/d , two types of vortices are dominant flow structures in

the wake region. One is tip vortices generated near side edges at the top face of the column, and the other is base vortices generated near the bottom plane. On the other hand, for large H/d , vortex streets are generated at mid-height of the column and interact strongly with the tip and the base vortices. Wang *et al.* (2006) pointed out that strong shear in a boundary layer enhances the base vortices and updraughts behind the column which weaken the tip vortices. Park and Lee (2002) also performed experiments on flow structures around a finite-height circular column in boundary layers with various wind profiles and found that vortex formation is strongly influenced by shear in boundary layers.

While flow structures behind a finite-height column have been well investigated, pollutant dispersion behind the column has only received attention recently (Rossi *et al.*, 2010; Gousseau *et al.*, 2012; Rossi and Iaccarino, 2013). According to Rossi and Iaccarino (2013), periodic fluctuations of pollutant concentration occur in the wake region due to vortex streets, and they affect turbulent fluxes of pollutant in the streamwise, spanwise and vertical directions. Nonetheless, there has been little study on pollutant dispersion behind high-rise buildings in real urban areas where other buildings affect flow around high-rise buildings (Hanna and Chang, 2015; Kwak *et al.*, 2015). Therefore, it is worth investigating turbulent flow and pollutant dispersion behind high-rise buildings in real urban areas.

Recently, large-eddy simulation (LES) models have been widely used to investigate turbulent flow and pollutant dispersion in real urban areas. An LES study by Xie and Castro (2009) on turbulent flow in a real urban area found that Reynolds stress and root-mean-square velocity fluctuations reach maximum at the top of high-rise buildings. Letzel *et al.* (2012) studied air ventilation at pedestrian level in Hong Kong and found that local ventilation is improved by vertical flow around a high-rise building. Nakayama *et al.* (2011) and Kanda *et al.* (2013) suggested new aerodynamic parametrizations for real urban surfaces and showed that the variability of building heights is crucial for the aerodynamic parametrizations. Nakayama *et al.* (2011) and Kanda *et al.* (2013) also insisted that because high-rise buildings increase the variability of building heights significantly, aerodynamic parametrizations in urban areas perform poorly if contributions of high-rise buildings to drag formation are not well considered. Nozu and Tamura (2012) investigated pollutant dispersion in a real urban area where many high-rise buildings exist and found that time-averaged mean concentration in the wake regions does not change significantly in the vertical direction due to strong updraughts behind the high-rise buildings. Furthermore, they mentioned that vortex shedding and intermittent air entrainment occur in the wake boundary regions leading to fluctuations of pollutant concentration. Park *et al.* (2015a) performed an LES on turbulent flow in a real urban area and found that vortices appear behind high-rise buildings and interact strongly with updraughts in the turbulent wake regions. All of these LES studies, however, did not analyse in detail vortex streets behind high-rise buildings.

Especially, there are very few studies on the relationship between vortex streets and pollutant dispersion.

In this article, we extend the study of Park *et al.* (2015a) by focusing on vortex streets behind high-rise buildings to investigate impacts of vortex streets on turbulent flow and pollutant dispersion in a real urban area. In section 2, an LES model and simulation design are described. In section 3, simulation results are presented and discussed. A summary and conclusions are presented in section 4.

2. LES model and simulation design

In this study, we use the parallelized LES model (PALM) 3.10 version (Letzel *et al.*, 2008; Maronga *et al.*, 2015). In PALM, equations of the filtered momentum, mass continuity, and passive scalar transport under the Boussinesq approximation are solved. The equation of subgrid-scale (SGS) turbulent kinetic energy is solved to parametrize the SGS fluxes (Deardorff, 1980). A finite difference method and a staggered Arakawa C-grid are used for spatial discretization. A fifth-order upwind scheme for the advection terms (Wicker and Skamarock, 2002) and a third-order Runge–Kutta scheme for time integration are used. PALM shows good performances in simulating wind fields in idealized building arrays (Razak *et al.*, 2013) and a real city (Park *et al.*, 2015b). Additional PALM validation over a staggered array of idealized buildings is performed. It is found that the normalized vertical profiles of mean streamwise velocity and velocity variances agree well with data of the wind-tunnel experiment over a building array (Cheng and Castro, 2002), in general. The evaluated profiles are available in the Supporting Information provided with this article (Figure S1).

Simulation settings used in this study are similar to those of Park *et al.* (2015a). Here, we choose an urban area in Seoul, South Korea, where buildings are densely built up. Figure 1 shows an elevation field of the computational domain. The size of the computational domain is $4320 \text{ m} \times 1440 \text{ m} \times 1040 \text{ m}$ in the x –(east–west), y –(south–north), and z –(vertical) directions, and the number of grid points is $864 \times 288 \times 132$. Here, z represents the height above sea level. The horizontal grid size is 5 m, and the thinnest and widest streets in the computational domain are resolved by 1 grid cell and about 9 grid cells, respectively. The vertical grid size is 5 m up to $z = 250 \text{ m}$ and increases algebraically by a factor of 1.08 up to $z \sim 325 \text{ m}$. Above $z \sim 325 \text{ m}$, the vertical grid size is 10 m. The grid resolutions of this study are equal to those of Park *et al.* (2015b) whose results match well with observation data. Two idealized simulations with a square tall building above a flat surface are performed to evaluate the grid resolution effects. The grid resolutions in the simulations are 5 and 2.5 m. Both cases show similar mean flow around and behind the building, although side wall recirculation zones of the building are not captured well in the 5 m resolution case. Also, the vertical profiles of vertical turbulent momentum flux and

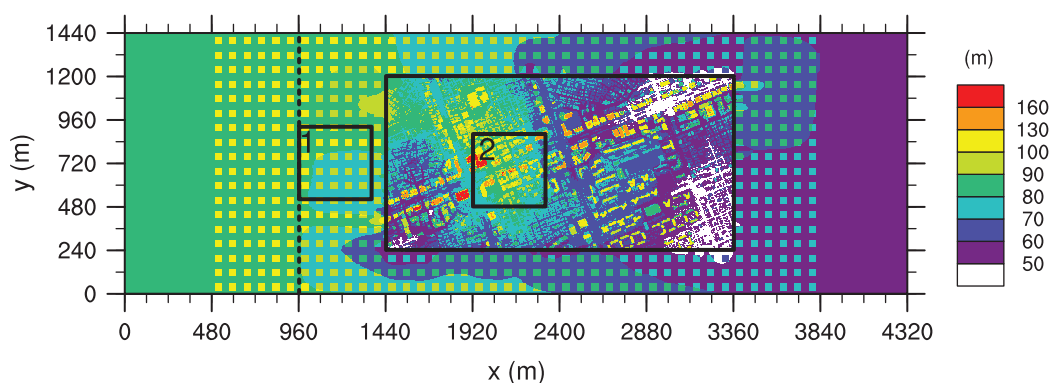


Figure 1. Elevation field (m) of the computational domain. The inner rectangle with a black solid line indicates the main domain of interest. Regions 1 and 2 represent the upstream and downstream areas of the high-rise buildings, respectively. Black dashed line located at $x = 960 \text{ m}$ indicates the location of the y – z plane pollutant emission source.

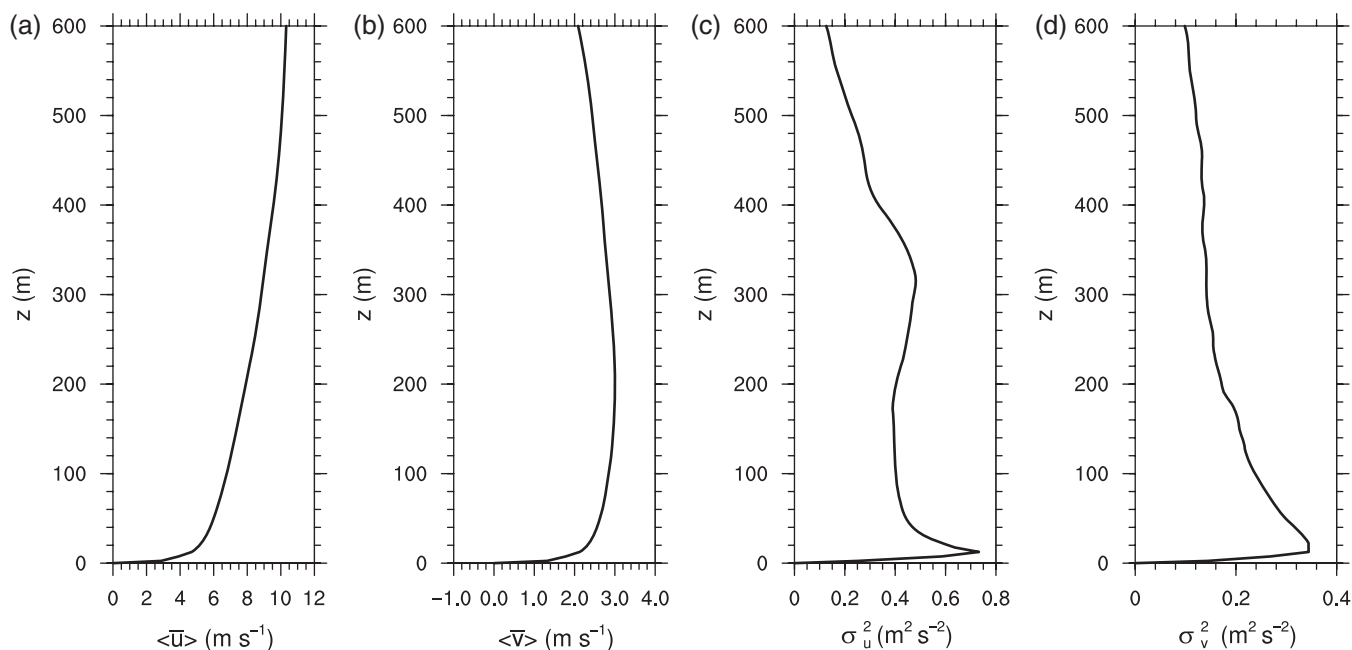


Figure 2. Horizontally and temporally averaged vertical profiles of velocities (m s^{-1}) in the (a) x -direction and (b) y -direction, and variances of velocities ($\text{m}^2 \text{s}^{-2}$) in the (c) x -direction and (d) y -direction.

turbulent kinetic energy (TKE) in the 5 m resolution case agree fairly well with those in the 2.5 m resolution case. Except near the ground, the ratio of temporally and horizontally averaged subgrid-scale TKE to temporally and horizontally averaged grid-scale TKE in the 5 and 2.5 m resolution cases are less than 0.06 and 0.04, respectively. Although the ratio in the 2.5 m resolution case is smaller than that in the 5 m resolution case, the 5 m resolution case can resolve most of the eddies induced by the square tall building. Thus, we speculate that the 5 m resolution would be reasonable for our purpose, although simulations with higher resolution in the real urban area are not performed due to computing resource limitation. The vertical profiles of the turbulence statistics are available in the Supporting Information provided with this article (Figure S2).

The main domain of interest is indicated by a black solid line, ranging from $x = 1440$ to 3360 m and from $y = 240$ to 1200 m. Digital elevation data are used to generate 5 m gridded elevation data of the main domain. The mean height and height standard deviation in the main domain are 71 m above sea level and 20 m, respectively. The plan area density of the main domain is 0.49. In the main domain, we focus particularly on turbulent flow and pollutant dispersion in the wake regions behind two high-rise buildings located at $(x, y) \sim (1870 \text{ m}, 540 \text{ m})$ and $(1920 \text{ m}, 740 \text{ m})$. For convenience, these are named building A and building B, respectively. Their heights are 206 and 167 m above the ground level, respectively. Region 1, located upstream of the main domain, is compared with region 2, located downstream of the high-rise buildings, to investigate turbulent characteristics of the wakes behind the high-rise buildings. Outside the main domain, buffer regions are added to maintain continuity of the elevation at the lateral boundaries of the main domain. Regular arrays of buildings are added in the buffer regions to maintain turbulence intensity (Park *et al.*, 2015a). The height and width of the array buildings are 20 and 40 m, respectively.

To generate realistic flow, the turbulence recycling method (Lund *et al.*, 1998; Kataoka and Mizuno, 2002; Park *et al.*, 2015a) is used. At each time step, inflow data at the west boundary ($x = 0$ m) are produced by adding turbulent signals and time-invariant inflow vertical profiles. The turbulent signals are calculated by subtracting a line average along the y -direction on the y - z plane at $x = 480$ m from original variables on the same y - z plane. The inflow vertical profiles and initial turbulence are obtained from a precursor simulation. For the precursor

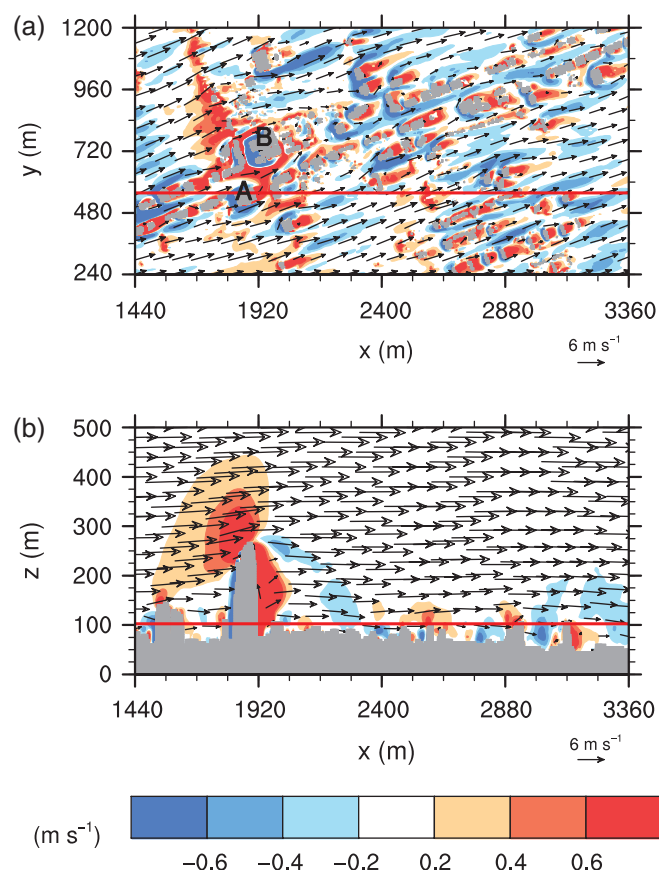


Figure 3. (a) Fields of mean horizontal velocity vector and vertical velocity (colour) on the x - y plane at $z = 102.5$ m. (b) Fields of mean velocity vector and vertical velocity (colour) on the x - z plane at $y = 557.5$ m. The red lines in (a) and (b) indicate the y and x positions of cross-section in (b) and (a), respectively.

simulation, westerly geostrophic wind at a speed of 10 m s^{-1} is initially imposed on a flat surface. The mean wind direction turns clockwise as the height increases due to the Coriolis force and the surface friction force. As a result, southwesterly wind becomes the dominant mean wind direction in the precursor simulation. The precursor simulation is conducted for 10 h, and horizontally and temporally averaged vertical profiles of the last 30 min simulation data are used as the inflow vertical profiles

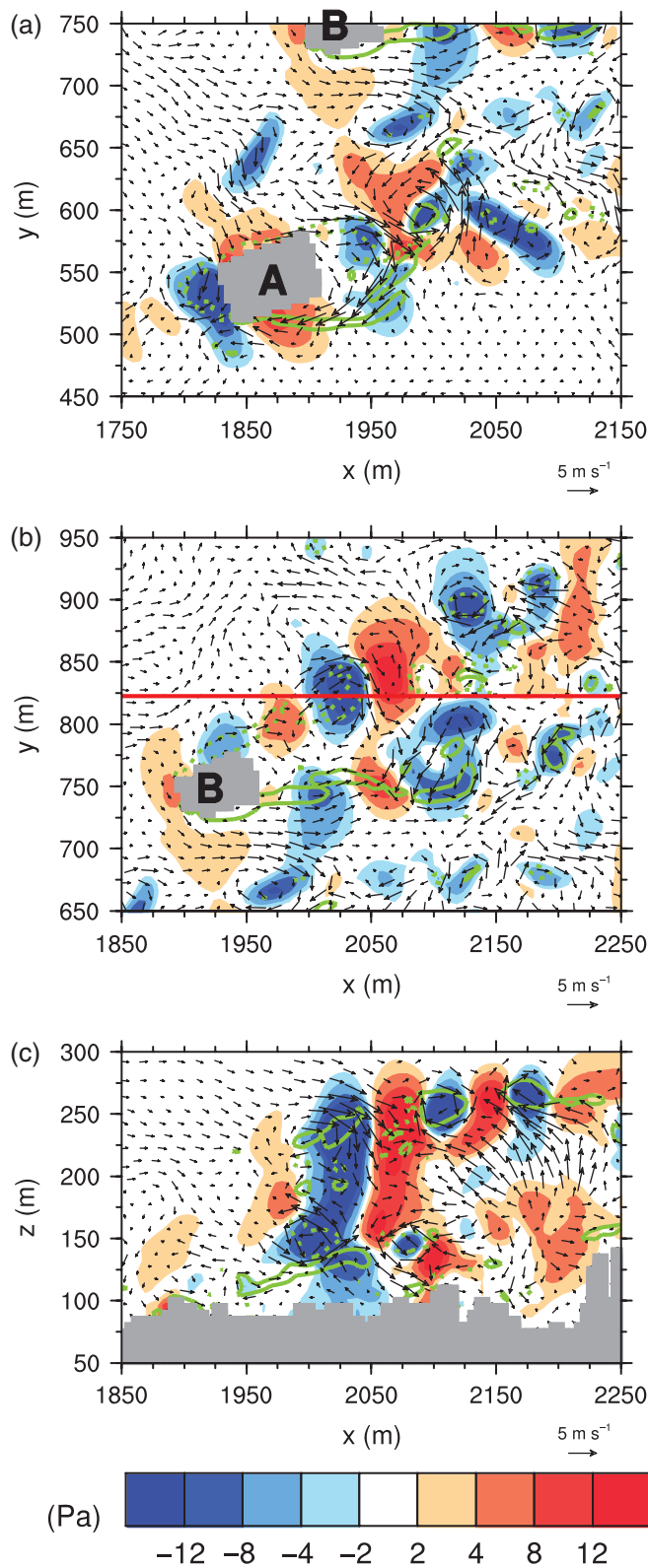


Figure 4. Fields of instantaneous velocity perturbation vector and pressure perturbation (Pa, colour) (a, b) on the x - y plane at $z=197.5$ m and (c) on the x - z plane at $y=822.5$ m at $t=3056$ s. The red line in (b) indicates the cross-section line for (c). Green contour lines in (a, b) and (c) represent the vorticities in the z - and y -directions (ω_z and ω_y), respectively; solid and dashed lines represent contours with values 0.45 and -0.45 s^{-1} , respectively.

of the main simulation (Park *et al.*, 2015a). Figure 2 shows the calculated vertical profiles of velocities and velocity variances. Here, u and v represent velocities in the x - and y -directions, respectively. Overbar and angle bracket denote temporal and horizontal averages, respectively. σ_u^2 and σ_v^2 represent variances of velocities in the x - and y -directions, respectively. The velocity in the x -direction increases with height, and the velocity in the y -direction decreases above $z \sim 200$ m. The velocity variances

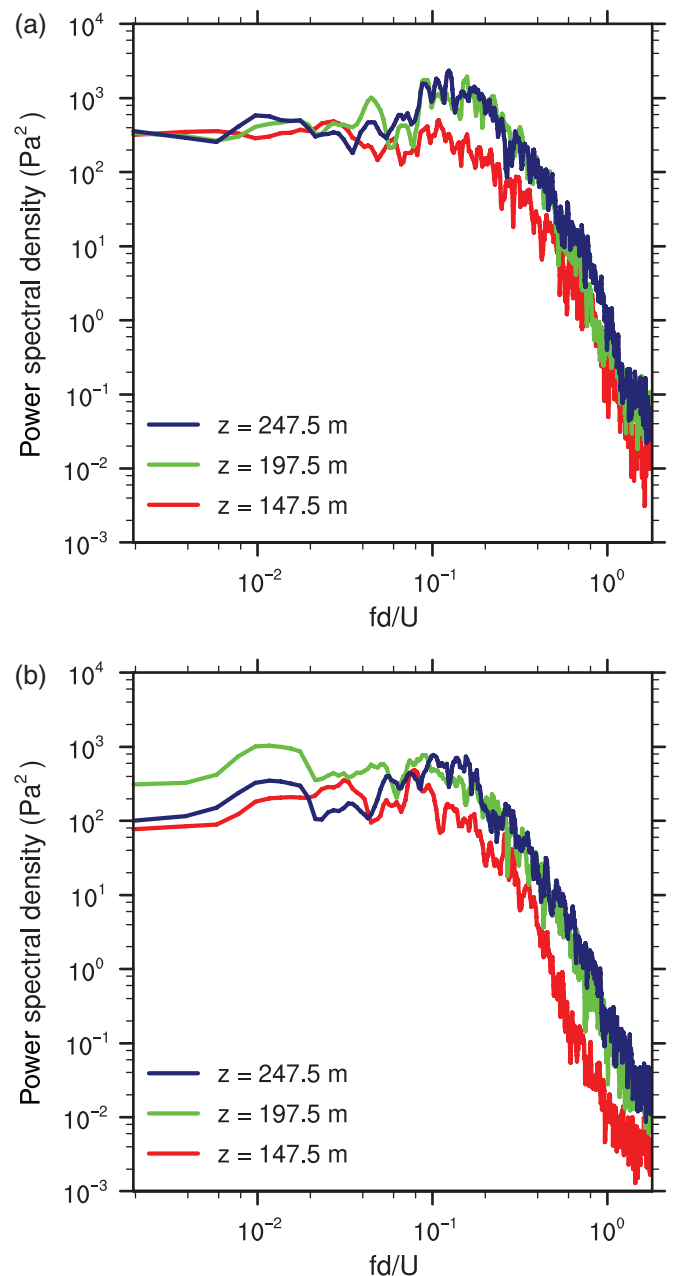


Figure 5. Power spectral densities of pressure perturbation at different heights $z = 247.5$ (blue), 197.5 (green), and 147.5 m (red) at points (a) $(x, y) = (2037.5$ m, 827.5 m) and (b) $(x, y) = (2077.5$ m, 757.5 m).

have maxima near the surface and then decrease with height in general.

At the east boundary ($x=4320$ m), the radiation boundary condition is imposed for velocity and the Neumann boundary condition for scalar concentration. At the south boundary ($y=0$ m) and north boundary ($y=1440$ m), the cyclic boundary condition is imposed for velocity and scalar concentration. At the top boundary ($z=1040$ m), the Dirichlet boundary condition is imposed for velocity and the Neumann boundary condition for scalar concentration. The Monin–Obukhov similarity with a roughness length of 0.1 m is used at the bottom and building surfaces for the velocity components (Park *et al.*, 2015a). In this study, the thermodynamic energy equation is not considered. A flat surface is in front of the east boundary to avoid counter flow which can stop the model run due to the radiation boundary condition at the outflow boundary. For pollutant dispersion, a passive scalar is emitted from the y - z plane source at $x=960$ m with a uniform scalar flux $5 \text{ g m}^{-2} \text{ s}^{-1}$. After the precursor simulation, additional integration over 1 h is performed, and simulation data of the last 30 min are analysed in this article.

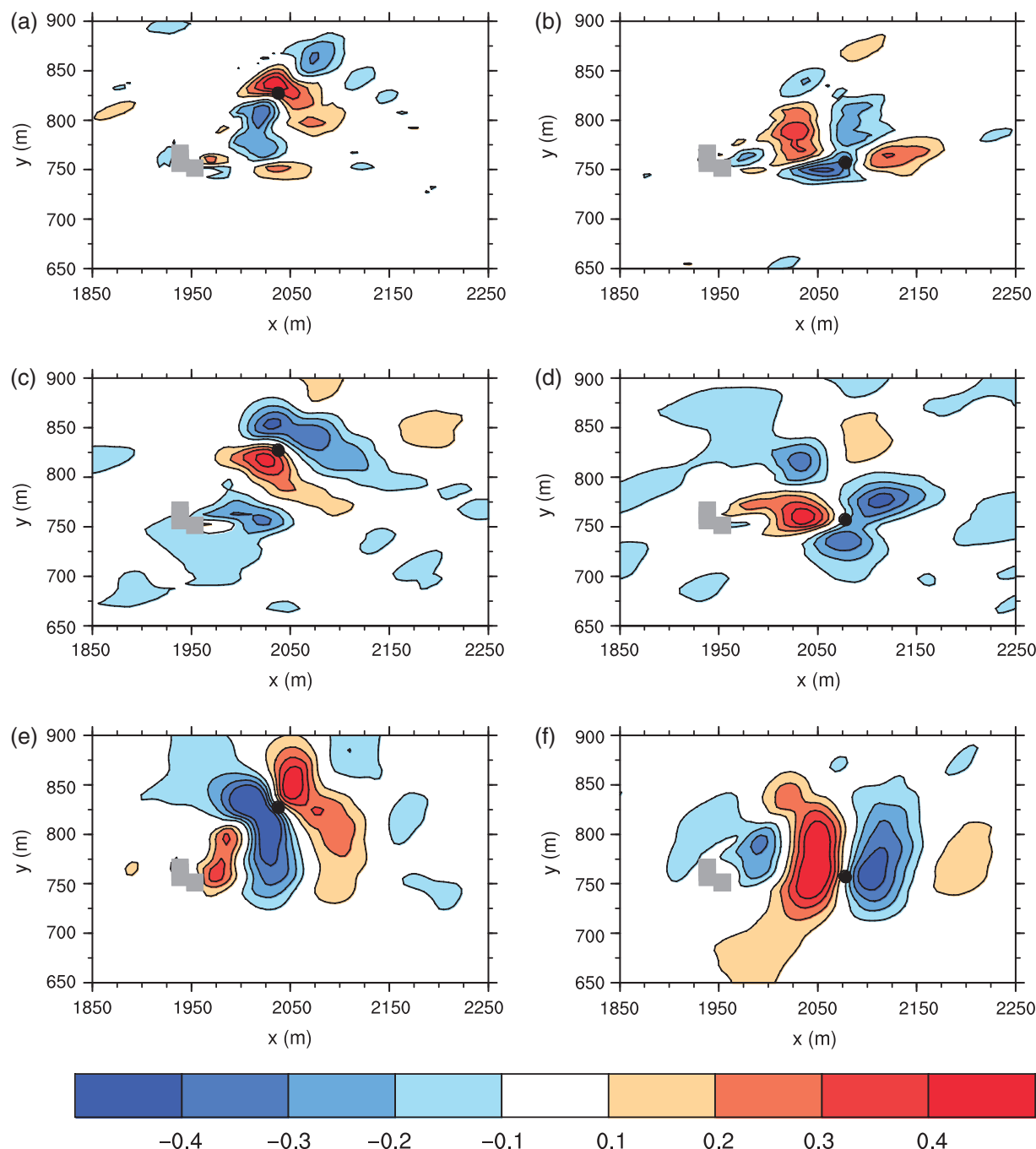


Figure 6. Correlation fields on the x - y plane at $z = 247.5$ m for (a, b) $R(p, \omega_z)$, (c, d) $R(p, u)$, and (e, f) $R(p, v)$ with reference points at (a, c, e) $(x, y) = (2037.5, 827.5)$ m and (b, d, f) $(x, y) = (2077.5, 757.5)$ m. The black dots indicate the reference points.

3. Results and discussion

3.1. Vortex streets and turbulence characteristics

Time-averaged mean velocity vector and vertical velocity fields on the x - y and x - z planes are analysed. The time average is taken for the last 30 min. Mean horizontal velocity vector and vertical velocity fields at $z = 102.5$ m, which is above the average height of the main domain ($z \sim 71$ m), are presented in Figure 3(a). We clearly see that updraughts and downdraughts occur strongly behind and in front of the buildings, respectively. Particularly in the region where buildings are densely built up ($x = 1800$ – 2160 m, $y = 600$ – 840 m), strong updraughts and downdraughts are observed. Such strong vertical motions are also well observed in the vertical plane at $y = 557.5$ m (Figure 3(b)). Also, updraughts and downdraughts are strong behind and in front of high-rise building A. These flow patterns are similar to what has been observed around a finite-height column (Wang *et al.*, 2004; Palau-Salvador *et al.*, 2010).

Fields of instantaneous velocity perturbation vector and pressure perturbation on the x - y plane at $z = 197.5$ m and x - z plane at $y = 822.5$ m at $t = 3056$ s are shown in Figure 4. Vorticity contours are also indicated in Figure 4. In this article, we define the perturbation α' as a deviation of an original variable α from the time-averaged variable $\bar{\alpha}$ ($\alpha' = \alpha - \bar{\alpha}$). In Figures 4(a) and (b), we see that clockwise vortices are generated on the northern side of high-rise buildings A and B while anticlockwise vortices are generated on their southern side. Here, vorticities in the z -direction near clockwise and anticlockwise vortices are generally negative and positive, respectively. It is also observed that pressure perturbations near the vortices are mostly negative. These vortices propagate downstream behind the high-rise buildings and form vortex streets. It is observed that when compared to the vortex streets from building B, the vortex streets from building A do not appear clearly due to disturbances from buildings in the upstream area of building A. This is clearly seen in the fields of pressure perturbation contours. On the vertical plane, both anticlockwise and clockwise vortices appear behind the high-rise buildings and

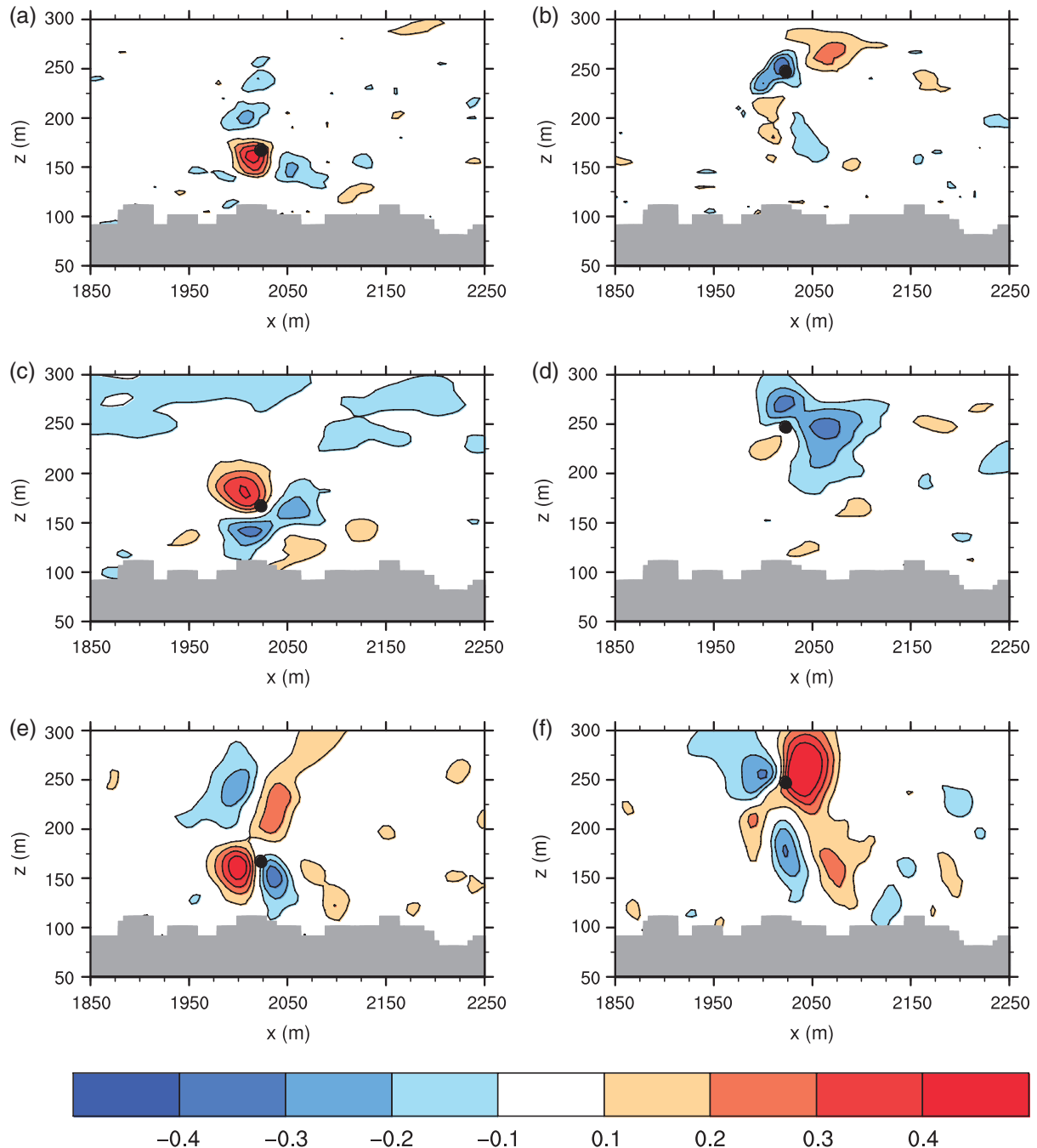


Figure 7. Correlation fields on the x - z plane at $y = 832.5$ m for (a, b) $R(p, w_y)$, (c, d) $R(p, u)$, and (e, f) $R(p, w)$ with reference points at (a, c, e) $(x, z) = (2022.5, 167.5)$ m and (b, d, f) $(x, z) = (2022.5, 247.5)$ m. The black dots indicate the reference points.

pressure perturbations near the vortices are also mostly negative (Figure 4(c)). Here, vorticities in the y -direction near clockwise and anticlockwise vortices are generally positive and negative, respectively.

To further investigate characteristics of the vortex streets, the power spectral density of pressure perturbation is calculated at three different heights ($z = 147.5, 197.5$ and 247.5 m) at points $(x, y) = (2037.5, 827.5)$ m and $(2077.5, 757.5)$ m (Figure 5). These points are located in the wake region behind high-rise building B. The power spectral density is plotted as a function of the non-dimensional frequency fd/U where f is the dimensional frequency, d is the width of high-rise building B normal to the wind direction (35 m), and U is the free stream velocity which is equal to the initially imposed geostrophic wind speed (10 m s^{-1}). Figure 5(a) shows that the power spectral density has peaks in the frequency range $fd/U = 0.1$ – 0.2 , similar to the results of idealized experiments (Sumner *et al.*, 2004; Bourgeois *et al.*, 2011). However, the peaks in Figure 5(a) are broader than those in other studies because turbulent disturbances from other buildings perturb flow around building B and interrupt the

periodic formation of vortices. Also, a broad peak can appear in the power spectrum when a fully turbulent boundary layer envelops a column (Huber, 1988). We see that the peaks at $z = 197.5$ and 247.5 m in Figure 5(b) are not clear compared to those in Figure 5(a). This seems to be due to interruption of the periodic formation of vortices by turbulent disturbance from a building located at $(x, y) \sim (1970, 720)$ m which is tall with a height of approximately 110 m and is very close to building B. The peak at $z = 147.5$ m in Figure 5(b) is clearer than that in Figure 5(a) because of the vortex street behind the building located at $(x, y) \sim (1970, 720)$ m.

As displayed in Figure 4, vortices appear frequently in the regions of negative pressure perturbation as observed in another study (Saeedi *et al.*, 2012). The relation between vortices and pressure perturbation can be investigated quantitatively by the two-point time-averaged correlation $R(\alpha, \beta)$ defined as:

$$R(\alpha(\mathbf{x}), \beta(\mathbf{y})) \equiv \frac{\overline{\alpha'(\mathbf{x})\beta'(\mathbf{y})}}{\sqrt{\overline{(\alpha'(\mathbf{x}))^2}}\sqrt{\overline{(\beta'(\mathbf{y}))^2}}}, \quad (1)$$

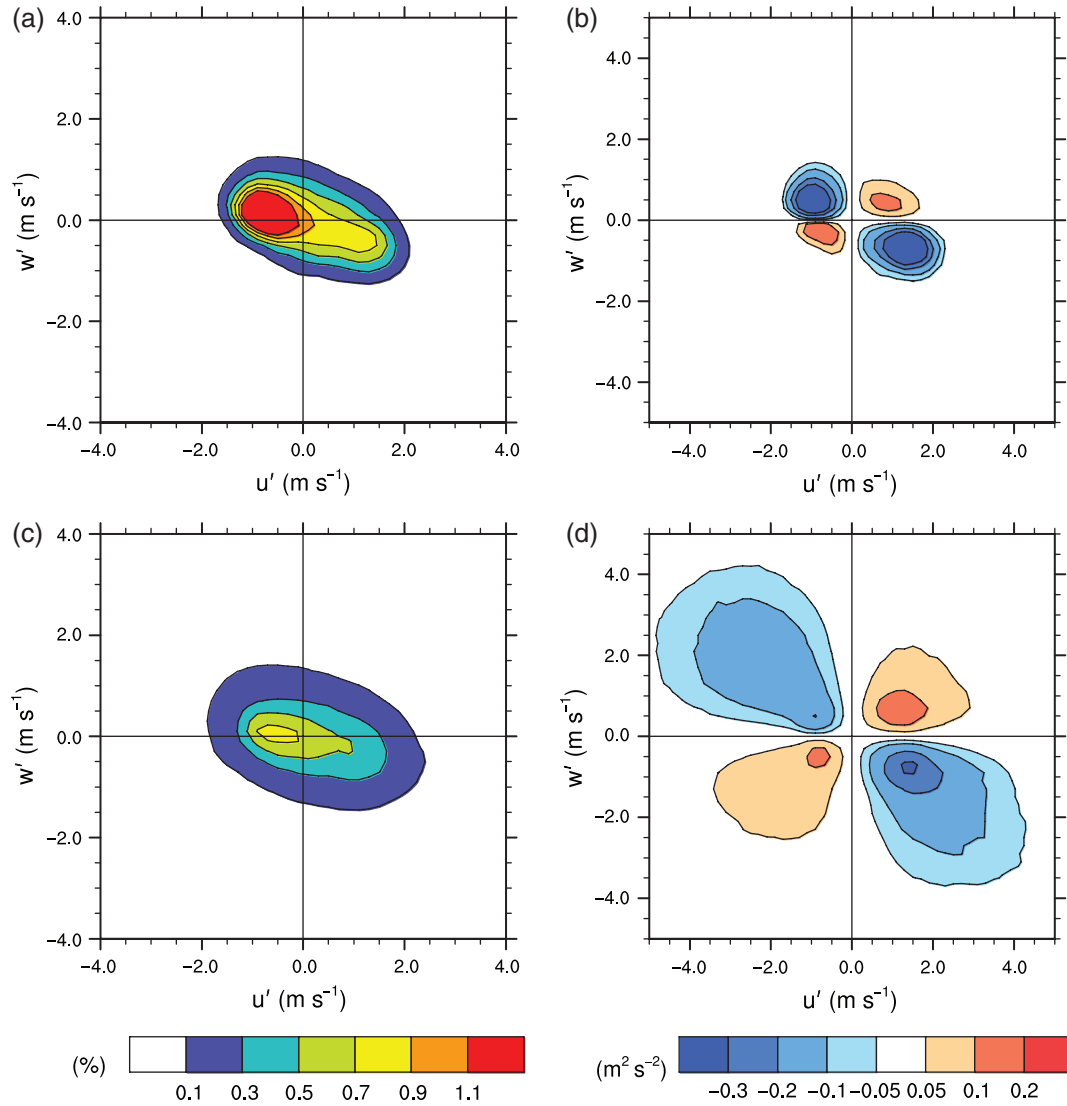


Figure 8. (a, c) Fields of the joint probability density function of u' and w' and (b, d) fields of the joint probability function of u' and w' multiplied by $u'w'$ in (a, b) region 1 and (c, d) region 2. The data at $z = 247.5$ m are used.

where $\alpha'(\mathbf{x}) = \alpha(\mathbf{x}) - \overline{\alpha(\mathbf{x})}$ and $\beta'(\mathbf{y}) = \beta(\mathbf{y}) - \overline{\beta(\mathbf{y})}$. Here, α and β are variables of interest, \mathbf{x} is the location of a reference point, \mathbf{y} is the location of the variable of interest β , the overbar denotes the time average, and the prime denotes the perturbation. Using Eq. (1), we compute a correlation between perturbation of the variable α at the reference point \mathbf{x} and perturbation of the variable β at the location \mathbf{y} .

Figure 6 shows correlation fields of $R(p, \omega_z)$, $R(p, u)$, and $R(p, v)$ on the x - y plane at $z = 247.5$ m at two reference points $(x, y) = (2037.5 \text{ m}, 827.5 \text{ m})$ and $(2077.5 \text{ m}, 757.5 \text{ m})$ on the northern and southern sides of the wake region of building B, respectively. Here, p represents the pressure, and ω_z denotes vorticity in the z -direction. By observing simulation results, we carefully chose the two reference points where clockwise and anticlockwise vortices frequently pass, respectively. In this way, these reference points can be indications of centres of vortices. The correlation can be interpreted as follows: because $R(p, \omega_z)$ is positive in Figure 6(a) around the reference point $(x, y) = (2037.5 \text{ m}, 827.5 \text{ m})$ where clockwise vortices with $\omega_z < 0$ pass, the pressure perturbation at this reference point is negative with a correlation value of approximately 0.4. This interpretation works for $R(p, u)$ and $R(p, v)$ as well in such a way that the correlation is zero at the reference point while there are strong positive and negative correlations around the reference point as shown in Figures 6(c) and (e). Similarly, we see in Figure 6(b) that $R(p, \omega_z)$ is negative at the reference point $(x, y) = (2077.5 \text{ m}, 757.5 \text{ m})$ where anticlockwise vortices with $\omega_z > 0$ pass so that the pressure perturbation at this reference point is negative. The

correlation value at the reference point is -0.3 . $R(p, u)$ and $R(p, v)$ in Figures 6(d) and (f) also confirm the correlations between the vortices and the negative pressure perturbation.

Correlations of $R(p, \omega_y)$, $R(p, u)$ and $R(p, w)$, are also investigated on the x - z plane at $y = 832.5$ m at two reference points at $(x, z) = (2022.5 \text{ m}, 167.5 \text{ m})$ and $(2022.5 \text{ m}, 247.5 \text{ m})$ in Figure 7. Here, w represents velocity in the z -direction, and ω_y denotes vorticity in the y -direction. Similar to Figure 6, the two reference points correspond to the points where anticlockwise and clockwise vortices frequently pass, respectively. In Figures 7(a) and (b), positive and negative values of $R(p, \omega_y)$ imply that pressure perturbation at these reference points is negative due to the anticlockwise and clockwise vortices, respectively. This is confirmed by the correlations $R(p, u)$ and $R(p, w)$ in Figures 7(c)–(f). Therefore, we can conclude that the vortices and the negative pressure perturbation have correlations with a value of approximately 0.4. Correlation fields near high-rise building A are also checked. Their correlations are less than those near building B due to interruption by disturbances from low-rise buildings around high-rise building A.

Now we investigate the effect of high-rise buildings A and B on vertical turbulent momentum flux using the joint probability density function (JPDF) of velocity perturbations u' and w' which is defined as:

$$f_{u', w'}(a_i, a_j) = P(a_i - 0.5\Delta a < u' \leq a_i + 0.5\Delta a, a_j - 0.5\Delta a < w' \leq a_j + 0.5\Delta a), \quad (2)$$

where a_i and a_j are the centres of bins and Δa is the spacing of bins (for more details, refer to Park and Baik (2013) and Park *et al.* (2015a)). Figure 8 shows fields of the JPDP of u' and w' and fields of the JPDP multiplied by $u'w'$ on the x - y plane at $z = 247.5$ m in region 1 (Figures 8(a) and (b)) and in region 2 (Figures 8(c) and (d)). Region 1 and region 2 are located upstream of the main domain and downstream of the high-rise buildings, respectively (Figure 1). The number of bins for u' and w' is 50, and Δa is 0.2 m s^{-1} . In region 1, the most dominant events are found in the second and fourth quadrants where ejections ($u' < 0, w' > 0$) and sweeps ($u' > 0, w' < 0$) occur, respectively (Figure 8(a)). These two main events transport momentum downward (Figure 8(b)). Region 2 also has dominant events of ejections and sweeps (Figure 8(c)) but in a wider area of the field (Figure 8(d)), which indicates that stronger events occur more frequently and contribute more significantly to the vertical turbulent momentum flux in region 2. Additionally, the contribution of ejections to the total vertical turbulent momentum flux increases significantly compared to that in region 1. In region 1, the vertical turbulent momentum fluxes induced by ejections and sweeps contribute 55 and 75% of the total vertical turbulent momentum flux, respectively, while in region 2, the vertical turbulent momentum fluxes induced by ejections and sweeps contribute 86 and 79% of the total vertical turbulent momentum flux, respectively. These results are consistent with those of Park *et al.* (2015a) for turbulent flow in a densely built-up urban area. However, results of the JPDP under different wind conditions and urban morphologies can be different from these results.

Figure 9 shows instantaneous fields of $\text{sgn}(w') \times \max(0, -u'w')$ on the x - z plane. Here, only ejection and sweep events are shown with positive and negative values, respectively (Park *et al.*, 2015a). Black contour lines represent contours of negative pressure perturbation with -6 Pa which can be an indication of vortices. Figure 9(a) shows that a vortex located at an upper level ($x, z \sim (2100 \text{ m}, 275 \text{ m})$) induces an ejection event. Also, Figure 9(b) shows that a vortex located at an upper level ($x, z \sim (2110 \text{ m}, 260 \text{ m})$) induces an ejection event, and the ejection event is stronger than that in Figure 9(a). This is because in Figure 9(b), updraughts under the vortex, which is located at $(x, z) \sim (2100 \text{ m}, 225 \text{ m})$, enhance the ejection. Similarly, Figure 9(c) shows that an upper-level vortex located at $(x, z) \sim (2140 \text{ m}, 240 \text{ m})$ induces a stronger ejection compared to that in Figure 9(a) because an anticlockwise vortex at a lower level at $(x, z) \sim (2125 \text{ m}, 160 \text{ m})$ enhances the ejection. Therefore, we see that ejections can be induced by upper-level vortices and enhanced by updraughts and lower-level vortices. As a result, ejections become the most dominant event as confirmed in Figure 8.

In the simulation, buildings have artificial stair-stepped walls to coincide with grid edges. Therefore, the effects of the stair-stepped walls on the simulated flow need to be examined. To evaluate the effects of the artificial stair-stepped walls, two idealized simulations with a square tall building above a flat surface are performed. One simulation considers the square tall building coincided with the grid mesh (coincided case), and the other simulation considers the square tall building rotated 30° (rotated case). Here, the square tall building in the rotated case has the artificial stair-stepped walls due to the 30° rotation. Inflow perpendicular to a front face of the building is considered in both cases. It is found that the mean flow patterns around and behind the building in the coincided and rotated cases show some differences such as flow asymmetry and weak backflow behind the building in the rotated case. However, important mean flow patterns such as decrease of wind speed behind the building and strong updraughts and downdraughts behind and in front of the building appear in both cases. It is also found that detailed turbulent flow patterns and vortex street characteristics in the rotated case are somewhat different from those in the coincided case. However, the vortex streets behind the building and the periodic vortex generation appear in both cases generally. Thus,

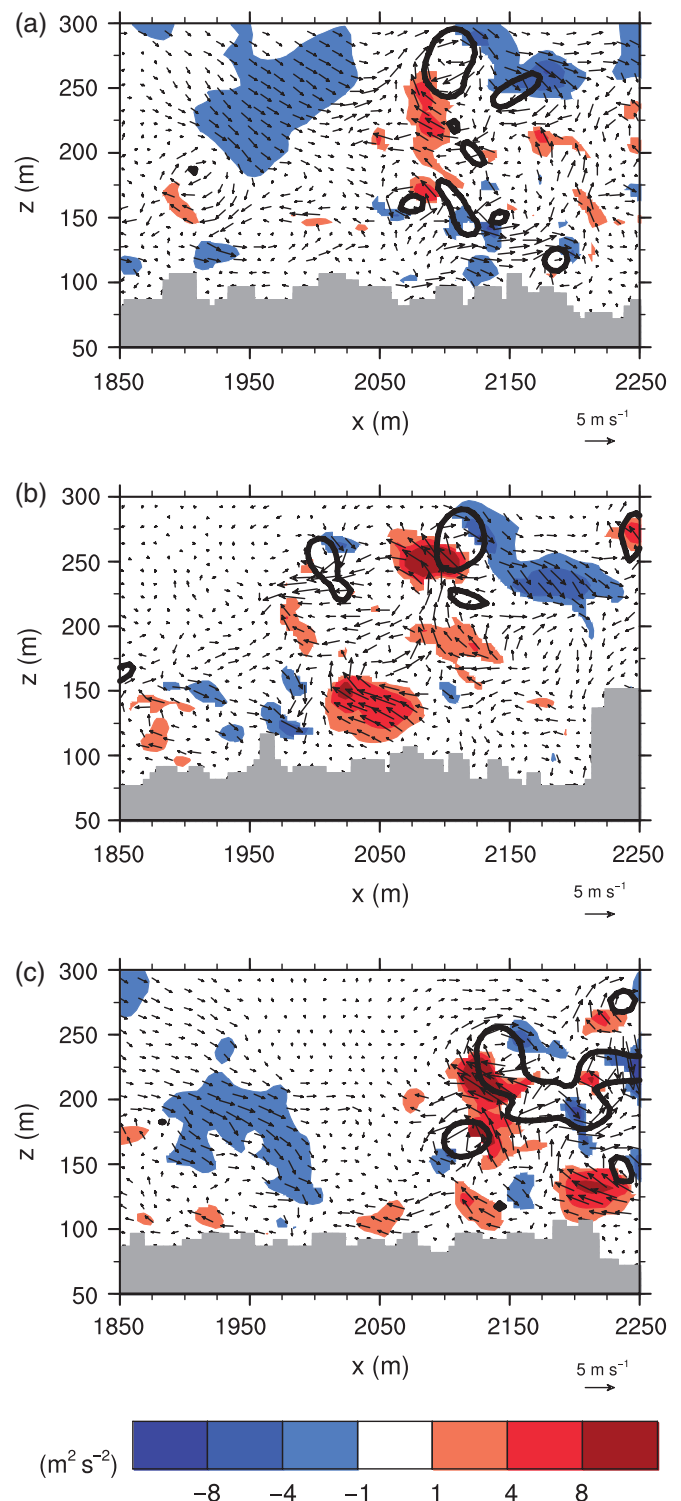


Figure 9. Fields of velocity perturbation vector and $\text{sgn}(w') \times \max(0, -u'w')$ on the x - z plane at (a) $y = 832.5 \text{ m}$ at $t = 3360 \text{ s}$, (b) $y = 812.5 \text{ m}$ at $t = 3008 \text{ s}$, and (c) at $y = 882.5 \text{ m}$ at $t = 3592 \text{ s}$. Black contour lines represent the contours of pressure perturbation with the contour level -6 Pa .

we speculate that the effects of the artificial stair-stepped walls can modify the mean and turbulent flows in the simulation for the real urban area, but the main findings of this study (e.g. periodic vortex shedding behind the high-rise buildings interrupted by other buildings) would not be changed significantly. The mean flow, turbulent quantities, and power spectral density in the coincided and rotated cases are available in the Supporting Information provided with this article (Figures S3–S5).

Two idealized simulations are compared to get an insight into the effects of the low-rise buildings on turbulent flows near the high-rise buildings. The setting of one simulation is the same as that of the coincided case. The setting of the other simulation is the same as that of the coincided case except the morphology of

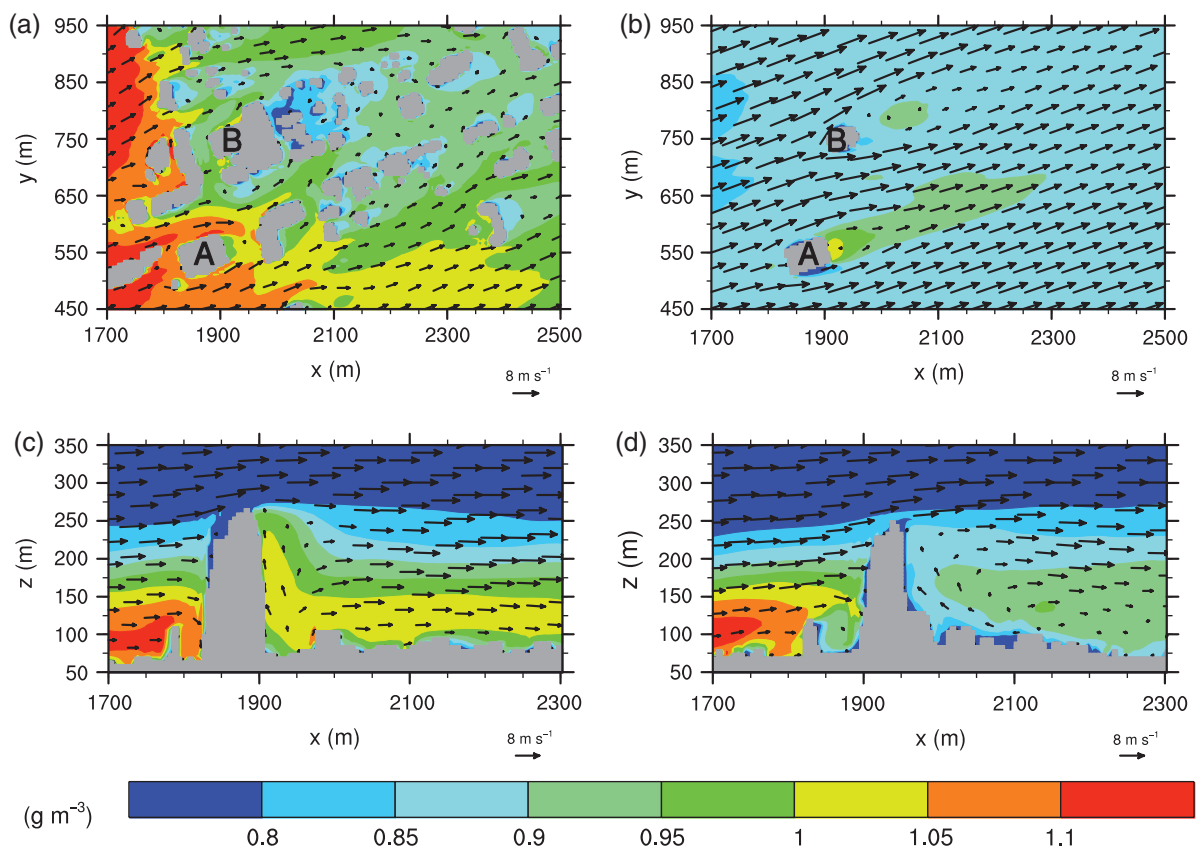


Figure 10. Fields of mean velocity vector and mean pollutant concentration (g m^{-3} , colour) on the x - y plane at (a) $z = 102.5$ m and (b) $z = 207.5$ m and on the x - z plane at (c) $y = 557.5$ m and (d) $y = 762.5$ m. A pollutant is emitted from the y - z plane source at $x = 960$ m.

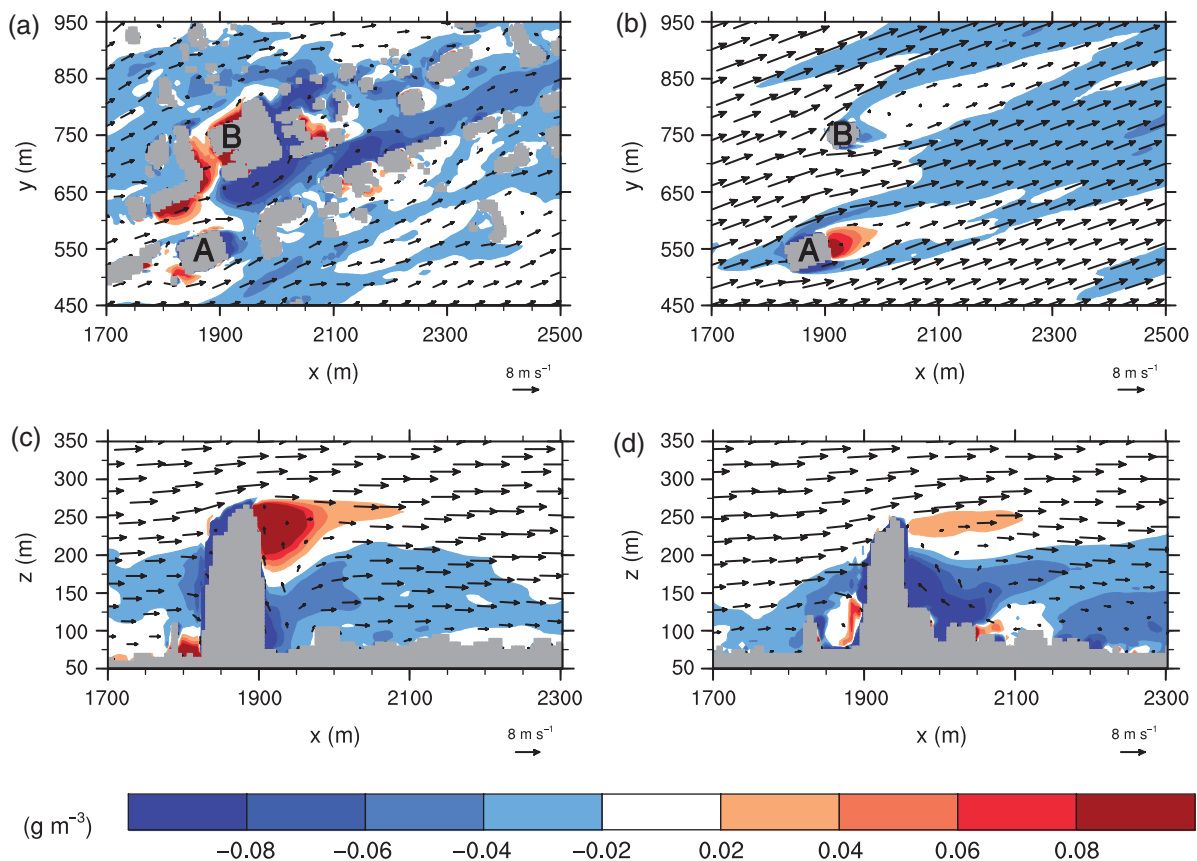


Figure 11. Fields of mean velocity vector of the original simulation and mean concentration difference (colour) between the simulations with and without the high-rise buildings on the x - y plane at (a) $z = 102.5$ m and (b) $z = 207.5$ m and on the x - z plane at (c) $y = 557.5$ m and (d) $y = 762.5$ m. A pollutant is emitted from the y - z plane source at $x = 960$ m.

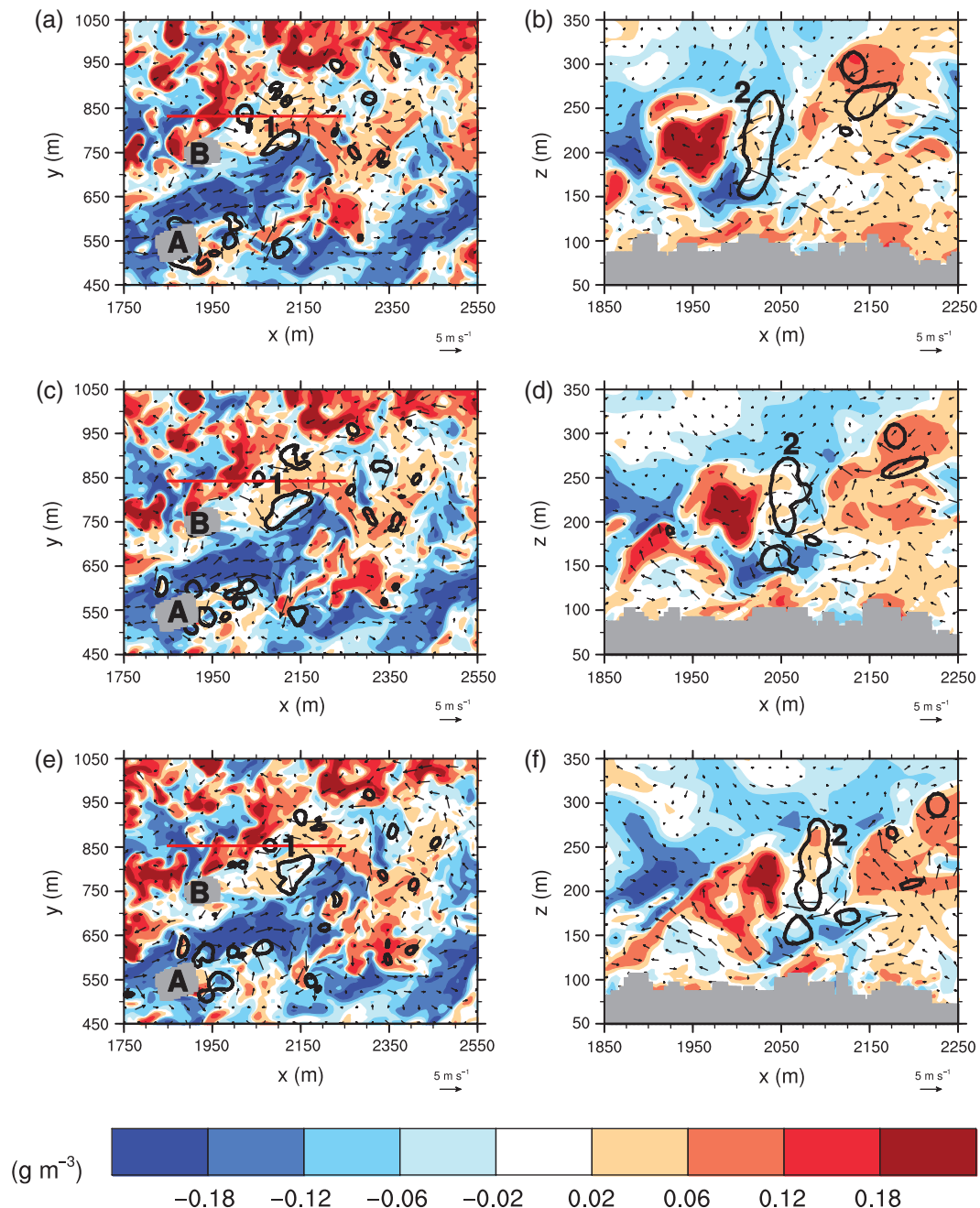


Figure 12. Fields of velocity perturbation vector and pollutant concentration perturbation (colour) on the x - y plane and the x - z plane (a) at $z = 197.5$ m and $t = 3306$ s, (b) at $y = 832.5$ m and $t = 3306$ s, (c) at $z = 197.5$ m and $t = 3312$ s, (d) at $y = 842.5$ m and $t = 3312$ s, (e) at $z = 197.5$ m and $t = 3318$ s, and (f) at $y = 852.5$ m and $t = 3318$ s. A red line in (a), (c), and (e) indicates the cross-section line for (b), (d), and (f), respectively. The black contour lines represent the pressure perturbation with the contour level -6 Pa.

the bottom surface (a square tall building and a low-rise cube building array). Above the mid-height of the square tall building, the idealized simulation with the square tall building and the low-rise building array exhibits broader peaks in the power spectral density of pressure perturbation, but the effects of the low-rise building array on mean and turbulent flows around and behind the square tall building are not significant. In the main domain, small street canyons with one grid box across exist, and flows in the small street canyons may not be resolved well. However, the idealized simulation results with low-rise buildings reveal that flows above the mid-height of the tall building are not so sensitive to the low-rise buildings. Therefore, we speculate that the impacts of the small street canyons on turbulent flows in the wake regions above the mid-height of the tall buildings, our main interest in this study, are not significant. An in-depth investigation through high-resolution simulations with the real urban morphology is needed to better understand the effects of the low-rise buildings on turbulent flows near the high-rise buildings.

3.2. Pollutant dispersion

In this section, we investigate pollutant dispersion in the main domain to examine effects of high-rise buildings. In the simulation, a passive scalar is emitted from the y - z plane source to consider a pollutant which is transported from other areas. Figure 10 shows time-averaged mean velocity vector and mean pollutant concentration fields on the x - y and x - z planes. At $z = 102.5$ m, transport of pollutant is interrupted by buildings, thus the mean concentration decreases significantly downstream of the buildings (Figure 10(a)). In particular, the mean concentration downstream of building B is much lower than that in other regions. On the other hand, the mean concentration at $z = 207.5$ m behind buildings A and B is higher than the mean concentration in other regions (Figure 10(b)). This is due to effects of pollutant accumulation due to low wind speed behind the high-rise buildings and pollutant transport by updraughts behind the high-rise buildings as seen from the vertical distributions of the mean pollutant concentration in Figures 10(c) and (d). The

pollutant transported by the updraughts consequently increases the concentration in the upper region, similar to what has been reported by other studies (Heist *et al.*, 2004; Gowardhan *et al.*, 2007; Nozu and Tamura, 2012). Below $z \sim 150$ m, the pollutant concentration behind building B (Figure 10(d)) is lower than that behind building A (Figure 10(c)) because pollutant dispersion is strongly interrupted by densely built-up low-rise buildings in front of high-rise building B as shown in Figure 10(a). Therefore, upward transport of pollutant behind building B does not increase significantly the pollutant concentration in the upper region.

To investigate effects of high-rise buildings more clearly, an additional simulation without high-rise buildings is conducted. In the additional simulation, the building close to building B (located at $(x, y) \sim (1970 \text{ m}, 720 \text{ m})$) and high-rise buildings A and B are removed, and the height of the terrain is replaced by the mean height in the main domain ($z \sim 71$ m). Figure 11 shows fields of mean velocity vector of the original simulation and fields of differences in the mean concentration between the two simulations. Positive and negative values of the concentration difference mean an increase and a decrease of the mean concentration due to the high-rise buildings, respectively. At $z = 102.5$ m, the concentration increases in front of high-rise building B because air ventilation is interrupted by building B (Figure 11(a)). On the contrary, the concentration decreases south of building B because updraughts occur south of building B (Figure 3(a)) and transport pollutant upward. At $z = 207.5$ m, there is less effect of the high-rise buildings on the concentration in general, but just behind building A, there is a significant increase in the concentration due to the upward transport of pollutant (Figure 11(b)). The increase of the concentration behind building A is also clearly displayed in Figure 11(c). Moreover, because strong updraughts transport pollutant from a low level to a high level behind high-rise buildings A and B, the concentration decreases in the wake region at the low level behind the high-rise buildings (Figures 11(c) and (d)).

Figure 12 shows instantaneous fields of perturbations of pollutant concentration and velocity vector on the x – y and x – z planes at three different times. Black contour lines represent contours of the negative pressure perturbation with -6 Pa as an indicator of vortices. In Figure 12, it is observed that frequent mixing occurs due to the vortices. For example, the anticlockwise vortex labelled as 1 in Figure 12 entrains air with low pollutant concentration from south to north where a region of high pollutant concentration exists (Figures 12(a), (c) and (e)). As a result, the magnitude of the pollutant concentration perturbation decreases (i.e. the pollutant is well-mixed) in this region. Similarly, in Figures 12(b), (d) and (f), the vortex labelled as 2 entrains air of low-concentration pollutant from the downstream area toward the high-concentration region. The role of vortices for mixing agrees with the results of Rossi and Iaccarino (2013) and Lodato and Rossi (2013) that perturbations induced by vortices play an important role in pollutant dispersion in all directions. It is also noticeable that below $z \sim 130$ m, black contour lines of negative pressure perturbation do not appear. This means that no vortex street is generated at low level ($z < 130$ m) and that concentration perturbation at the low level is not affected significantly.

Using the correlation between vorticity in the z -direction and concentration $R(\omega_z, c)$, we can also quantify relations between the vortices and the concentration perturbation. In Figure 13, two reference points are located at $(x, y) = (2037.5 \text{ m}, 827.5 \text{ m})$ and $(2077.5 \text{ m}, 757.5 \text{ m})$, the same as in Figure 6. In Figure 13(a), clockwise vortices ($\omega_z < 0$) pass the reference point. Thus, the correlation $R(\omega_z, c)$ can be interpreted in such a way that positive and negative values of $R(\omega_z, c)$ represent negative and positive values of the concentration perturbation, respectively. In Figure 13(b), anticlockwise ($\omega_z > 0$) vortices pass the reference point. Thus, the correlation $R(\omega_z, c)$ can be interpreted in such a way that negative and positive values of $R(\omega_z, c)$ represent negative and positive values of the concentration perturbation in Figure 13(b), respectively. We see in Figure 13(a) that

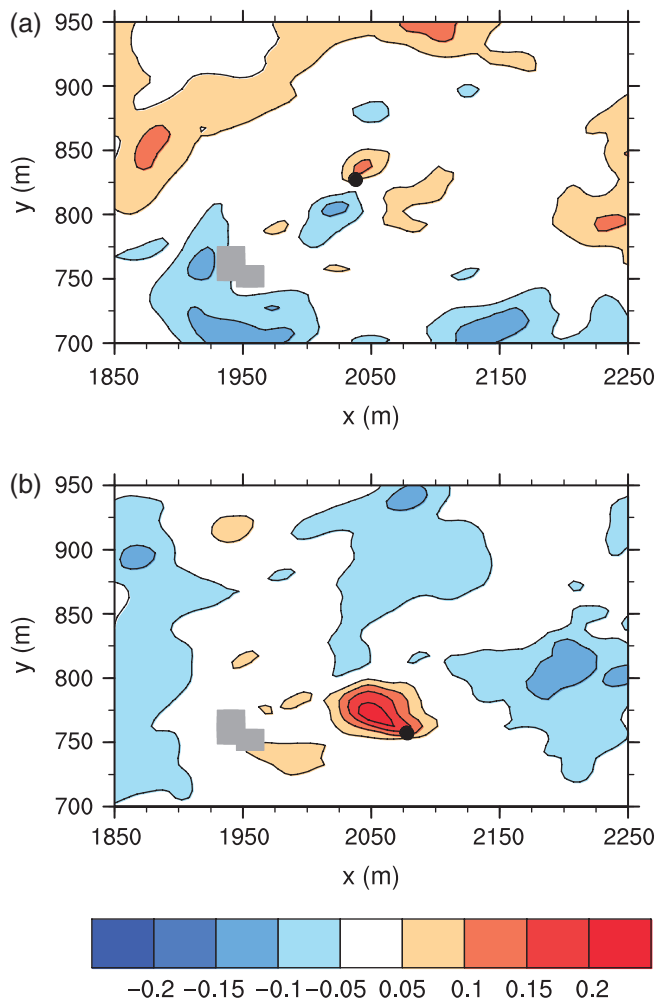


Figure 13. Correlation fields on the x – y plane at $z = 247.5$ m for $R(\omega_z, c)$ with reference points at (a) $(x, y) = (2037.5 \text{ m}, 827.5 \text{ m})$ and (b) $(x, y) = (2077.5 \text{ m}, 757.5 \text{ m})$. The black dots indicate the reference points.

values of $R(\omega_z, c)$ are negative and positive in the upstream and downstream areas of the reference point, respectively. At $z = 247.5$ m, the mean concentration is high in the wake region behind building B. Thus, as the clockwise vortex propagates downstream, it entrains the low-concentration air into the wake region while ejecting the high-concentration air of the wake region. This means that the concentration perturbation is positive and negative in the upstream and downstream areas of centres of the clockwise vortices, respectively, as shown by the correlation $R(\omega_z, c)$ with values of approximately 0.1. This implies that vortex streets are responsible for mixing in the wake region behind the high-rise buildings. However, the magnitude of $R(\omega_z, c)$ is small, implying that the relationship between the vortices and pollutant dispersion is less relevant and therefore more complex and irregular than the relationship between the vortices and pressure perturbation. This behaviour is similarly observed behind building A. However, in Figure 13(b), only positive values of $R(\omega_z, c)$ in the upstream area of the reference point appear, and the mixing behaviour by the vortices is not clearly observed. It seems that the building near building B (located at $(x, y) \sim (1970 \text{ m}, 720 \text{ m})$) interrupts mixing by the vortices.

4. Summary and conclusions

We investigated turbulent flow and associated pollutant dispersion in an approximated representation of a real urban area using an LES model. Urban flow structures, such as strong updraughts and downdraughts, turbulent wakes and vortex streets appear in front and downstream of the high-rise buildings. The non-dimensional vortex shedding frequency computed from

the power spectral density of pressure perturbation lies in the range of 0.1–0.2. This range agrees with previous studies in idealized situations, but the peaks are broader due to interruption by disturbances induced by other buildings. Also, we found that there is a correlation between pressure perturbation and vortices because vortices appear in regions of negative pressure perturbation. The vertical turbulent momentum flux was investigated by means of the joint probability density function of u' and w' . It was found that in the downstream area of the high-rise buildings, ejection and sweep are the main events and they become stronger in the wake region than in the upstream area. Especially, ejection is the most dominant event in the wake region because ejection is induced by upper-level vortices and strengthened by updraughts and lower-level vortices. At a low level, the mean pollutant concentration behind the high-rise buildings is low due to slow flow around the high-rise buildings. On the other hand, strong updraughts behind the high-rise buildings transport pollutant upward so that the mean pollutant concentration at an upper level increases behind the high-rise buildings. The vortex streets are responsible for mixing in such a way that the vortices eject air with high pollutant concentration in the wake region while they entrain air with low pollutant concentration into the wake region. The mixing by vortices was also confirmed quantitatively by correlations between the vorticity in the z -direction and the concentration. From the correlations, it was confirmed that the pollutant concentration perturbation is positive and negative in the places where air is ejected from and entrained into the wake region by the vortices, respectively.

Although this study presents detailed results on flow and pollutant dispersion associated with vortex streets in a real urban area, further simulation studies need to follow. For instance, this study does not consider different inflow wind profiles and turbulence intensities, urban surface heating, and thermal stratification, which can modify turbulent flow and associated pollutant dispersion. Also, the alignment angle, height and width of the regular arrays in the buffer region affect flow in the main domain. Therefore, these effects should be investigated in the future.

Acknowledgements

The authors are grateful to anonymous reviewers for providing valuable comments on this work. This work was supported by Mid-career Researcher Program through the National Research Foundation of Korea (NRF) grant funded by the Ministry of Science, ICT and Future Planning (MSIP) (No. 2016R1A2B2013549).

Supporting information

The following supporting information is available as part of the online article:

Figure S1. Normalized vertical profiles of temporally averaged (a) velocity in the x -direction ($\langle u \rangle$) and variances of (b) u (σ_u^2) and (c) w (σ_w^2). Dots denote data of the wind-tunnel experiment (Cheng and Castro, 2002). Here, h is the height of the array buildings, and u and w represent the velocities in the x - and z -directions, respectively. U_r is the free stream velocity. In the simulation, both the width and height of the idealized buildings are 40 m. The free stream velocity in the x -direction is 4.5 m s^{-1} , and the resolution of the simulation is 4 m.

Figure S2. Vertical profiles of temporally and area averaged (a) velocity in the x -direction, (b) vertical turbulent momentum flux, and (c) (resolved) turbulent kinetic energy (TKE) in the 5 and 2.5 m resolution cases. All quantities are averaged over an area behind the square tall building. u and w represent the velocities in the x - and z -directions, respectively. Overbar and square bracket denote the temporal and area averages, respectively. Prime denotes the perturbation from time average. In the simulations, the width and height of the square tall building are 50 and 200 m,

respectively, and the free stream velocity in the x -direction is 5 m s^{-1} .

Figure S3. Fields of mean horizontal velocity vector and the variable q ($= \sqrt{u^2 + v^2 + w^2}$, colour) on the x - y plane at $z = 150 \text{ m}$ in the (a) coincided and (b) rotated cases. Here, v represents the velocity in the y -direction. In the simulations, the width and height of the square tall building are 50 and 200 m, respectively, and the free stream velocity in the x -direction is 5 m s^{-1} .

Figure S4. Vertical profiles of temporally and area averaged (a) $\sqrt{u^2 + v^2}$, (b) $\sigma_u^2 + \sigma_v^2$, and (c) turbulent kinetic energy (TKE) in the coincided and rotated cases. All quantities are averaged over an area behind the square tall building. σ_u^2 and σ_v^2 represent the variances of u and v , respectively.

Figure S5. Power spectral densities of pressure perturbation at different heights: $z = 200$ (orange), 150 (blue), 100 (green), and 50 (red) m in the (a) coincided and (b) rotated cases. The power spectral densities in the coincided and rotated cases are calculated behind the square tall building.

References

- Bourgeois JA, Sattari P, Martinuzzi RJ. 2011. Alternating half-loop shedding in the turbulent wake of a finite surface-mounted square cylinder with a thin boundary layer. *Phys. Fluids* **23**: 095101. <https://doi.org/10.1063/1.3623463>.
- Britter RE, Hanna SR. 2003. Flow and dispersion in urban areas. *Ann. Rev. Fluid Mech.* **35**: 469–496.
- Cheng H, Castro IP. 2002. Near wall flow over urban-like roughness. *Boundary-Layer Meteorol.* **104**: 229–259.
- Deardorff JW. 1980. Stratocumulus-capped mixed layers derived from a three-dimensional model. *Boundary-Layer Meteorol.* **18**: 495–527.
- Edussuriya P, Chan A, Ye A. 2011. Urban morphology and air quality in dense residential environments in Hong Kong. Part I: District-level analysis. *Atmos. Environ.* **45**: 4789–4803.
- Fröhlich J, Rodi W. 2004. LES of the flow around a circular cylinder of finite height. *Int. J. Heat Fluid Fl.* **25**: 537–548.
- Gousseau P, Blocken B, van Heijst GJF. 2012. Large-eddy simulation of pollutant dispersion around a cubical building: Analysis of the turbulent mass transport mechanism by unsteady concentration and velocity statistics. *Environ. Pollut.* **167**: 47–57.
- Gowardhan AA, Pol SU, Brown MJ. 2007. 'Transport and dispersion phenomenon in urban areas: Measurement from the Joint Urban 2003 field experiment.' In *Proceedings of the 7th American Meteorological Society Conference on the Urban Environment*, 10–13 September 2007, San Diego, CA.
- Hanna S, Chang J. 2015. Skyscraper rooftop tracer concentration observations in Manhattan and comparisons with urban dispersion models. *Atmos. Environ.* **106**: 215–222.
- Heist DK, Perry SG, Bowker GE. 2004. 'Evidence of enhanced vertical mixing in the wakes of tall buildings in wind tunnel simulations of lower Manhattan'. In *Proceedings of the 5th American Meteorological Society Conference on the Urban Environment*, 23–26 August 2004. Vancouver, Canada.
- Heist DK, Brixey LA, Richmond-Bryant J, Bowker GE, Perry SG, Wiener RW. 2009. The effect of a tall tower on flow and dispersion through a model urban neighborhood, Part 1. Flow characteristics. *J. Environ. Monit.* **11**: 2163–2170.
- Huber AH. 1988. Video images of smoke dispersion in the near wake of a model building. Part I. Temporal and spatial scales of vortex shedding. *J. Wind Eng. Ind. Aerodyn.* **31**: 189–223.
- Kanda M, Inagaki A, Miyamoto T, Gryschka M, Raasch S. 2013. A new aerodynamic parametrization for real urban surfaces. *Boundary-Layer Meteorol.* **148**: 357–377.
- Kataoka H, Mizuno M. 2002. Numerical flow computation around aeroelastic 3D square cylinder using inflow turbulence. *Wind Struct.* **5**: 379–392.
- Kawamura T, Hiwada M, Hibino T, Mabuchi I, Kumada M. 1984. Flow around a finite circular cylinder on a flat plate (cylinder height greater than turbulent boundary layer thickness). *Bull. JSME* **27**: 2142–2151.
- Kwak K-H, Baik J-J, Ryu Y-H, Lee S-H. 2015. Urban air quality simulation in a high-rise building area using a CFD model coupled with mesoscale meteorological and chemistry-transport models. *Atmos. Environ.* **100**: 167–177.
- Letzel MO, Krane M, Raasch S. 2008. High resolution urban large-eddy simulation studies from street canyon to neighbourhood scale. *Atmos. Environ.* **42**: 8770–8784.
- Letzel MO, Helmke C, Ng E, An X, Lai A, Raasch S. 2012. LES case study on pedestrian level ventilation in two neighbourhoods in Hong Kong. *Meteorol. Z.* **21**: 575–589.
- Lodato G, Rossi R. 2013. 'Numerical investigation of scalar mixing in the turbulent wake of a square cylinder'. In *Proceedings of the 43rd Fluid Dynamics Conference*, 24–27 June 2013, San Diego, CA.

- Lund TS, Wu X, Squires KD. 1998. Generation of turbulent inflow data for spatially-developing boundary layer simulations. *J. Comput. Phys.* **140**: 233–258.
- Maronga B, Gryschka M, Heinze R, Hoffmann F, Kanani-Sühring F, Keck M, Ketelsen K, Letzel MO, Sühring M, Raasch S. 2015. The Parallelized Large-eddy Simulation Model (PALM) version 4.0 for atmospheric and oceanic flows: Model formulation, recent developments, and future perspectives. *Geosci. Model Dev.* **8**: 1539–1637.
- Nakayama H, Takemi T, Nagai H. 2011. LES analysis of the aerodynamic surface properties for turbulent flows over building arrays with various geometries. *J. Appl. Meteorol. Climatol.* **50**: 1692–1712.
- Nakayama H, Jurcakova K, Nagai H. 2013. Large-eddy simulation of plume dispersion within various actual urban areas. *Adv. Sci. Res.* **10**: 33–41.
- Nelson MA, Pardyjak ER, Klewicki JC, Pol SU, Brown MJ. 2007. Properties of the wind field within the Oklahoma City Park Avenue street canyon. Part I: Mean flow and turbulence statistics. *J. Appl. Meteorol. Climatol.* **46**: 2038–2054.
- Nozu T, Tamura T. 2012. LES of turbulent wind and gas dispersion in a city. *J. Wind Eng. Ind. Aerodyn.* **104–106**: 492–499.
- Palau-Salvador G, Stoesser T, Fröhlich J, Kappler M, Rodi W. 2010. Large eddy simulations and experiments of flow around finite-height cylinders. *Flow Turbul. Combust.* **84**: 239–275.
- Panagiotou I, Neophytou MK-A, Hamlyn D, Britter RE. 2013. City breathability as quantified by the exchange velocity and its spatial variation in real inhomogeneous urban geometries: An example from central London urban area. *Sci. Total Environ.* **442**: 466–477.
- Park C-W, Lee S-J. 2002. Flow structure around a finite circular cylinder embedded in various atmospheric boundary layers. *Fluid Dyn. Res.* **30**: 197–215.
- Park S-B, Baik J-J. 2013. A large-eddy simulation study of thermal effects on turbulence coherent structures in and above a building array. *J. Appl. Meteorol. Climatol.* **52**: 1348–1365.
- Park S-B, Baik J-J, Han B-S. 2015a. Large-eddy simulation of turbulent flow in a densely built-up urban area. *Environ. Fluid Mech.* **15**: 235–250.
- Park S-B, Baik J-J, Lee S-H. 2015b. Impacts of mesoscale wind on turbulent flow and ventilation in a densely built-up urban area. *J. Appl. Meteorol. Climatol.* **54**: 811–824.
- Razak AA, Hagishima A, Ikegaya N, Tanimoto J. 2013. Analysis of airflow over building arrays for assessment of urban wind environment. *Build. Environ.* **59**: 56–65.
- Rossi R, Iaccarino G. 2013. Numerical analysis and modeling of plume meandering in passive scalar dispersion downstream of a wall-mounted cube. *Int. J. Heat Fluid Fl.* **43**: 137–148.
- Rossi R, Philips DA, Iaccarino G. 2010. A numerical study of scalar dispersion downstream of a wall-mounted cube using direct simulations and algebraic flux models. *Int. J. Heat Fluid Fl.* **31**: 805–819.
- Rotach MW, Gryning S-E, Batchvarova E, Christen A, Vogt R. 2004. Pollutant dispersion close to an urban surface – the BUBBLE tracer experiment. *Meteorol. Atmos. Phys.* **87**: 39–56.
- Saeedi M, LePoudre P, Wang B-C. 2012. ‘Direct numerical simulation of flow around a surface-mounted square-section cylinder with AR = 4’. In *Proceedings of 20th Annual Conference of the CFD Society of Canada*, 9–11 May 2012, Canmore, Canada.
- Sattari P, Bourgeois JA, Martinuzzi RJ. 2012. On the vortex dynamics in the wake of a finite surface-mounted square cylinder. *Exp. Fluids* **52**: 1149–1167.
- Sumner D. 2013. Flow above the free end of a surface-mounted finite-height circular cylinder: A review. *J. Fluid Struct.* **43**: 41–63.
- Sumner D, Heseltine JL, Dansereau OJP. 2004. Wake structure of a finite circular cylinder of small aspect ratio. *Exp. Fluids* **37**: 720–730.
- Wang HF, Zhou Y. 2009. The finite-length square cylinder near wake. *J. Fluid Mech.* **638**: 453–490.
- Wang HF, Zhou Y, Chan CK, Wong WO, Lam KS. 2004. ‘Flow structure around a finite-length square prism’. In *Proceedings of the 15th Australasian Fluid Mechanics Conference*, 13–17 December 2004, Sydney, Australia.
- Wang HF, Zhou Y, Chan CK, Lam KS. 2006. Effect of initial conditions on interaction between a boundary layer and a wall-mounted finite-length-cylinder wake. *Phys. Fluids* **18**: 065106. <https://doi.org/10.1063/1.2212329>.
- Wicker LJ, Skamarock WC. 2002. Time-splitting methods for elastic models using forward time schemes. *Mon. Weather Rev.* **130**: 2088–2097.
- Xie Z-T, Castro IP. 2009. Large-eddy simulation for flow and dispersion in urban streets. *Atmos. Environ.* **43**: 2174–2185.